Fig. 1.18. Left: 3D visualization of the ostracod data with gray-scale segmentation of cuticle (cyan) and soft tissues (red). Right: Reconstructed slice of a sea urchin tooth fragment.
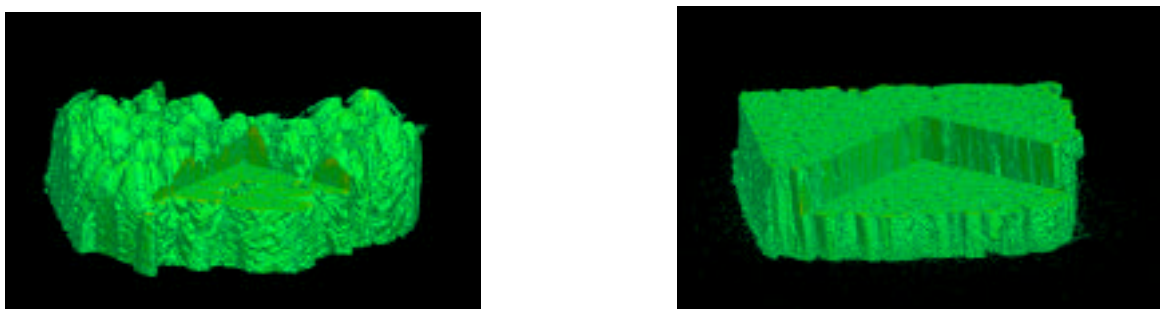

Fig. 1.19. Reconstructed 3D images of EBPVD-YSZ thermal barrier coatings. Left: Image showing structure at the top of the coating. Right: Image showing the structure of the same deposit at the substrate.

1.7 Diffraction and Coherent Scattering

Microdiffraction and coherent scattering methods that take advantage of high-resolution focusing optics and the APS brilliance are important components of the X-ray Microscopy Group user program. Recent highlights include diffraction imaging of antiferromagnetic domains, observation of columnar features in step-graded semiconductor films, combinatorial structure-property mapping of a binary alloy, phase-contrast imaging of defects in macro-molecular crystals, and measurement of x-ray speckle contrast shifts at absorption edges.

1.7.1 Microdiffraction Imaging of Antiferromagnetic Domains

Antiferromagnetic ordering refers either to existing interpenetrating sublattices of identical structure of local magnetic moments with opposite direction or to a zero total spin moment even though the spin density does not vanish. There have been few applications of antiferromagnets because the net magnetic moment is almost always zero at a practically accessible length scale and because they have been extremely difficult to image. We developed a new x-ray microdiffraction technique that makes it dramatically easier to map and analyze antiferromagnetic structure. We used it to reveal the broadening of the first-order "spin-flip" (SF) transition at 123 K in chromium, across which the spins rotate

by 90° at the walls between domains with orthogonal spin density wave (SDW) modulations (Evans et al., 2002).

Chromium is an antiferromagnet below the Néel transition at 311 K, in which the Coulomb interactions among electrons and the geometry of the Fermi surface conspire to produce incommensurate SDWs with modulation vectors that can lie along any of the three (001) axes of the unit cell. The SDW is accompanied by a lattice distortion and charge density wave (CDW) with a wave vector twice that of the SDW. In bulk Cr crystals, the orientation of spins relative to the wave vector of the SDW changes from transverse to longitudinal upon cooling through the SF transition. Combining nonresonant x-ray magnetic scattering with x-ray microdiffraction, we mapped the weak coupling between the long wavelength spin density modulation and the atomic-scale electron density modulation. A microfocused hard x-ray beam provided the high photon flux density necessary for weak magnetic scattering and the spatial resolution necessary for visualizing SDW domains. Figure 1.20 displays the SDW domains and their accompanying CDW domains in Cr at 130K. Figure 1.21 shows images of a single SDW domain at temperatures near the SF transition temperature. This first-order transition from transverse to longitudinal spin polarization results in the disappearance of magnetic scattering from the SDW domain due to the dependence of the scattering cross section on spin polarization. The SF transition begins at the boundary between SDW domains, revealing nucleation of a magnetic phase not at a structural grain boundary, as for the magnetic films, but at its magnetic equivalent. The interplay between macroscopically observable phenomena and the configuration of domains, both magnetic and ferroelectric, is increasingly important as density requirements in many technologies drive device feature sizes towards those of individual domains.
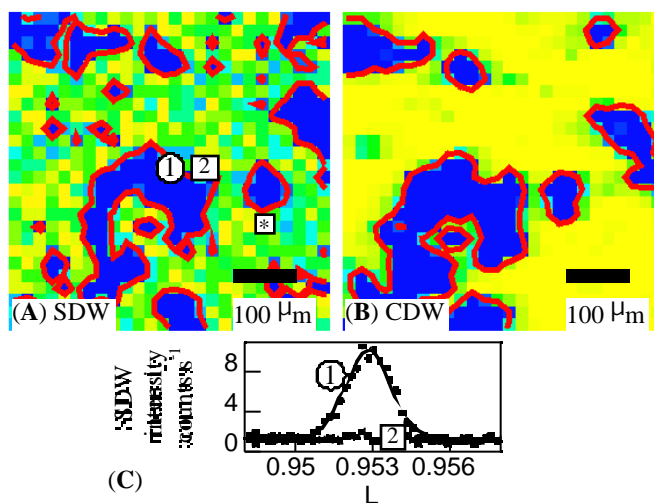

Fig. 1.20. Magnetic domains in Cr at T=130K. Intensity maps of the (A) SDW reflection and (B) CDW reflection from the same area of the Cr sample. (C) Reciprocal space scans at the positions indicated on the SDW map. The solid line is a Gaussian fit to the scan at position 1.
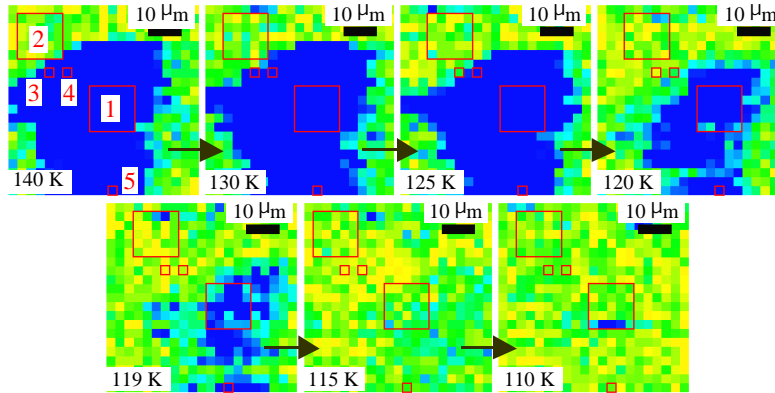
Fig. 1.21. Images of a single SDW domain at temperature near T_{SF}. This domain also appears at a different scale in Fig. 1 (marked with asterix).

1.7.2 Observation of Columnar Microstructure in Step-Graded $Si_{1-x}Ge_x$/Si Films

$Si_{1-x}Ge_x$/Si(001) heterostructures are used in high-speed bipolar transistors in communications applications and have potential for high-speed field effect transistors (FETs). Electron microscopy studies have shown that epitaxial $Si_{1-x}Ge_x$ layers with x < 0.5 on Si(001) relax by the introduction of 60° misfit dislocations, with misfit segments running in perpendicular (110) directions parallel to the wafer surface and terminating in threading arms that run up to the wafer surface. Compositionally graded $Si_{1-x}Ge_x$ buffer layers have low-threading dislocation densities (typically 10^5-10^7 cm^{-2}) and are therefore useful for FETs. Strain-relaxed epitaxial films, such as $Si_{1-x}Ge_x$/Si(001), exhibit mosaic broadening originating from the misfit dislocations that relieve the strain. Although x-ray diffraction measurements on step-graded relaxed $Si_{1-x}Ge_x$ films have revealed local tilted regions having the same lattice parameter ($\Delta d/d \approx 5 \times 10^{-4}$) and a range of tilt angles up to ~0.25°, the lateral dimension of the tilted regions could only be roughly estimated (<20 µm) until now.

We used x-ray microdiffraction with an incident beam of size 0.25-2.7 µm and divergence of 0.004°-0.05° to investigate the structure of $Si_{1-x}Ge_x$ films. A CCD detector was employed to map diffraction intensities as functions of sample position or individual micrograins in the and 2 scattering plane. Rocking scans indicated a complex variety of shapes and wide range of tilt angles. All spectra showed a complex fine structure on the 0.01 - 0.02° scale. We solved the microstructure by comparing the results from films with low- and high-misfit dislocation densities and using an iterative fitting algorithm (Eastman et al., 2002). Rectangular columnar micrograins were found with average widths ranging from 0.6 - 3.7 µm. The vast majority are between 0.8 µm and 1.4 µm, extending from the misfit dislocation network near the SiGe/Si interface up to the wafer surface. The micrograins had similar lattice parameters ($\Delta d/d \approx 5 \times 10^{-4}$), but their (001) axes were tilted up to ~0.1° with respect to the (001) axes of the Si substrate. Measured diffuse scattering, about 10-20% of the diffracted intensity, suggested the existence of a nonuniform strained material near the boundary regions between the micrograins.

1.7.3 Phase Contrast X-ray Diffraction Imaging of Defects in Biological Macromolecular Crystals

The substantial decrease in source size and divergence offered by third-generation synchrotron facilities has enabled us to develop a new phase-contrast x-ray diffraction method for imaging defects in protein crystals (Hu et al., 2001). This coherence-based method is extremely sensitive to lattice irregularities compared to conventional x-ray topography. It provides a new way to characterize structural defects and the causes of lattice disorder over a wide spectrum of macromolecular crystal systems.

Figure 1.22 shows a phase-contrast x-ray diffraction image of a well-faceted and optically defect-free tetragonal hen egg-white lysozyme crystal taken at the (440) reflection at beamline 2-BM. Several defects are discernible. Dislocations D, dislocation loops (or half loops) L, and additional structural features exhibited greater contrast as the sample-to-camera distance was increased. Linear features originate from the growth

sector boundary (GB at the top-right corner in figure). A number of defects also emerge from the center of the crystal and originate from the initial nucleus. The dislocation segments are largely along the <001> and <110> directions, yet subtle osmotic pressure might play a role in the dislocation configuration given the intrinsic nature of weak macromolecular bonding. The loop-like dislocations are attributed to stress/strain relief around stress centers, e.g., caused by nonuniform trapping of impurities. This work illustrates that lattice defects and irregularities in weakly scattering protein crystals can be effectively mapped by simply incorporating phase information of exit x-ray waves into diffraction imaging.

1.7.4 Continuous Structure-Property Mapping of Combinatorially Synthesized $Fe_{1-x}Ni_x$ Binary Alloys

Mapping of complex structural and physical property relationships as functions of material composition is traditionally accomplished through synthesis and analysis of samples with discrete compositions, prepared one at a
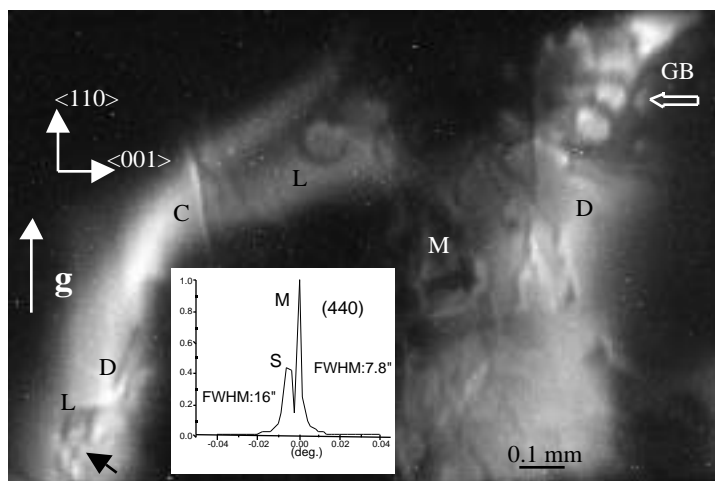

Fig. 1.22. Phase-contrast diffraction image of a hen egg-white lysozyme crystal; inset shows rocking curve. White regions diffract strongly. (g) Diffraction vector, (GB) growth sector boundary, (C) microcracks, (D) dislocation defect, (L) dislocation loop or half-loop.

time. This slow process limits detailed mapping, without which one may miss important opportunities in material discovery. At 2-BM, we are developing x-ray diffraction and fluorescence techniques to rapidly analyze combinatorial phase libraries.

To start, we mapped the well-documented $Fe_{1-x}Ni_x$ binary alloy system using a single composition-spread sample (Fig. 1.23) with x changing linearly from zero to one (Yoo et al., 2001). Its crystal structure and composition were determined by x-ray diffraction and fluorescence using a 50 μm beam oriented along the composition-spread direction. The $Fe_{1-x}Ni_x$ alloy system exhibited two dominant crystal structures: a Fe-rich, -phase with a body-centered-cubic (BCC) structure and a Ni-rich, -phase with a face-centered-cubic (FCC) structure with a rather broad two-phase overlap from x = 0.12 to 0.2. While both structures are rotationally epitaxial, the -phase alloys from x = 0.2 to 0.7 exhibited particularly excellent specular texture with better than 0.1° rocking curve width, which

suggests greater crystalline ordering than the alloys with other compositions. As shown in Fig. 1.24, the lattice constants for both phases satisfactorily reproduce those obtained from discrete bulk alloys, with minor discrepancies. First, the -phase retains much greater stability extending below x = 0.2, which can be attributed to a lower interfacial energy of the FCC film on the hexagonal substrate. Second, the lattice constant for the -phase is consistently smaller than the bulk values with the most significant deviation over the 0.5 < x < 0.8 region, which can be attributed to the large degrees of the residual strain in this region. The magnetic properties, measured by less than 200 μm, are also well correlated with the structures characterized by x-rays (see scanning Hall probe and scanning magneto-optical Kerr effect with a spatial resolution of Fig. 1.24). The $Fe_{1-x}Ni_x$ composition-spread sample exhibited good overall structural agreement with bulk Fe-Ni alloys, providing convincing evidence that the combinatorial synthesis can be efficiently used for structure-property mapping.
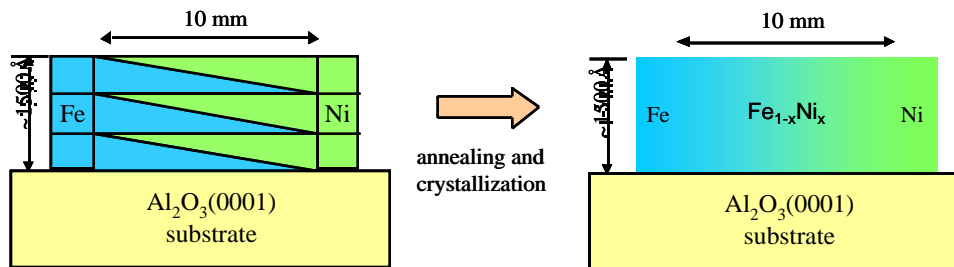

Fig. 1.23. Binary $Fe_{1-x}Ni_x$ composition-spread sample obtained by sputter-depositing thickness-gradient Fe/Ni multilayers at room temperature. As-grown multilayered films were annealed at 600°C for 3 h in evacuated ampoules, followed by air quenching, to obtain full compositional mixing normal to the film plane without oxidation and to achieve alloy phase formation.
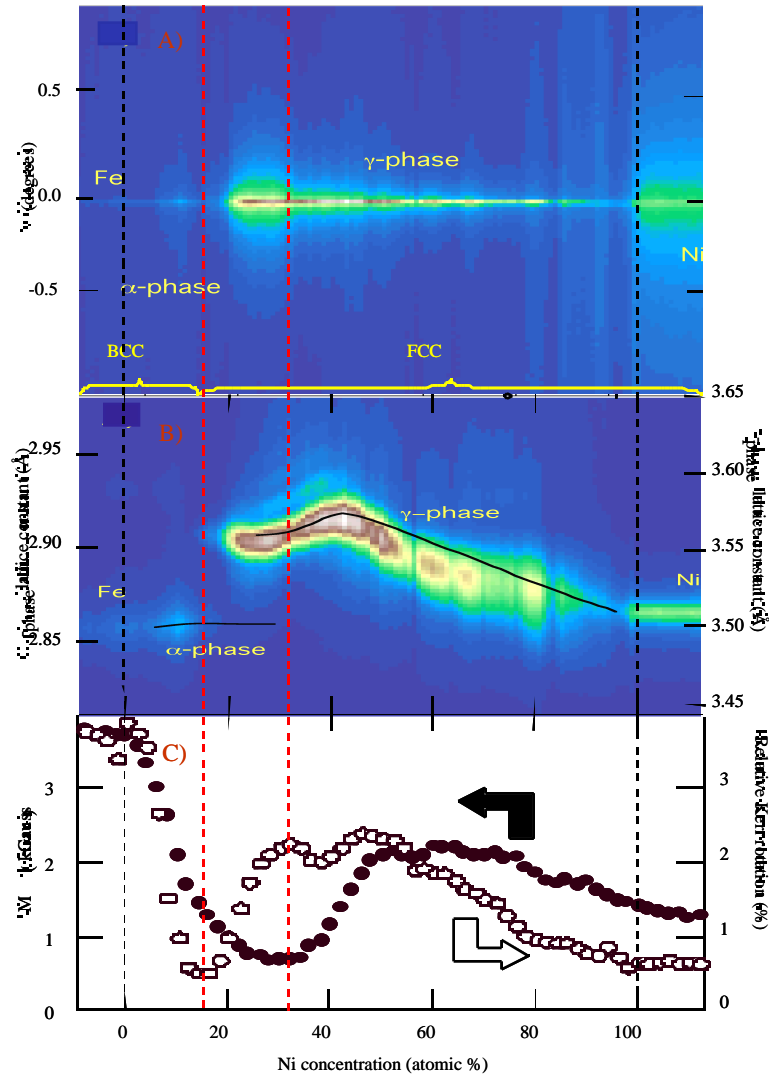
Fig. 1.24. (top) Structure-property map of the $Fe_{1-x}Ni_x$ sample. (middle) Specular texture of the composition-spread film obtained by   -rocking. The lattice constants were obtained from specular radial scans (bottom). Previously reported lattice constants obtained from discrete bulk alloys are shown as black lines for comparison. Red dashed lines show correlation of crystallographic structures with the magnetic properties. The regions below and above are the pure Fe and Ni phases, respectively.

1.7.5 X-ray Speckle Contrast Variation across Absorption Edges

X-ray speckle methods were introduced to the x-ray regime several years ago. At the 2-ID-B beamline, we are extending coherent scattering techniques, such as speckle, into the 1 to 4 keV range, which includes absorption edges in many important elements such as Al, Si, P, S, Zn, Ga, As, and the rare earths.

Coherent soft x-rays were recently used to probe the Gd M_5 (1190 eV) and Fe L_3 (707 eV) edges in resonant magnetic speckle experiments (Rahmim et al., 2002). Yet to our knowledge, the effect of absorption edges on x-ray speckle contrast has not yet been studied quantitatively. Standard speckle theory assumes that the energy dependence of the average intensity at a point in reciprocal space does not vary significantly over the

width of the spectral response function (Parry, 1984), and therefore does not predict any effect.

To test this, we recorded speckle data as a function of the incident x-ray energy across the Zn L_3 edge (1021 eV) in metallic zinc powder samples consisting of ~100 nm grains supported on 200-nm-thick silicon nitride membranes. The disordered powder samples were illuminated with a nearly (92%) coherent, 10-μm-diameter x-ray beam. We found by analyzing the intensity auto-correlation function of the data that the speckle contrast decreases as the absorption cross section increases at the edge (Fig. 1.25), indicating that standard speckle theory is indeed invalid near absorption edges (Retsch & McNulty, 2001). Speckle data taken across the K edge of a powdered aluminum sample (1560 eV) yielded comparable results. This effect has already been exploited to enhance speckle originating from a constituent element in a sample, e.g., to study ordering in anti-ferromagnetic domains. In addition to these
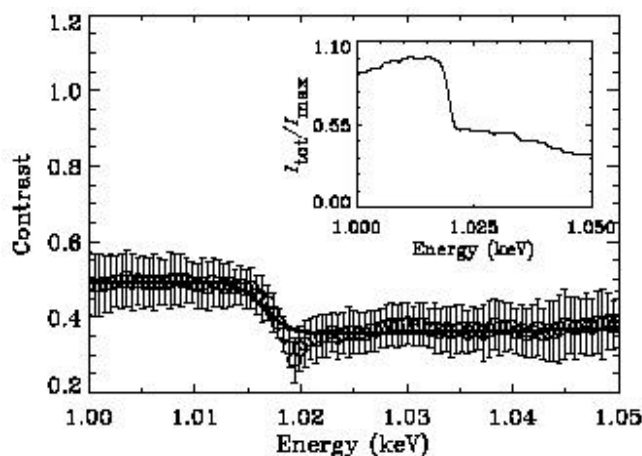

Fig. 1.25. X-ray speckle contrast versus energy in Zn powder (1.8-eV resolution), averaged over a small region of reciprocal space. The solid line shows a theoretical fit to the data points. Inset shows the total transmitted intensity measured directly behind the sample, normalized by the beamline efficiency.

applications, edge-dependent contrast variations should be well understood if pre-, on-, and post-edge measurements are to be compared in coherent scattering experiments.

1.8 New Techniques and Instrumentation

Several technical enhancements supported our activities. We acquired a state-of-the-art visible fluorescence microscope and developed a precision kinematic sample holder that enables correlative visible and x-ray microscope studies as well as fast positioning of specimens with 1 μm accuracy. The 2-ID-E fluorescence microprobe was upgraded with a motorized table and curved rails allowing rapid and repeatable energy changes. We developed a compact, modular soft x-ray "nanoprobe" that permits rapid and reproducible optics alignment in the soft x-ray scanning microscope and diffractometer. Other key instrumentation developments included a quantitative x-ray beam coherence diagnostic, commissioning of the 2-BM broad-band double-multilayer monochromator, a major upgrade of the fast microtomography system, integration of the hard x-ray microprobe with a six-circle diffractometer, and fabrication of high-aspect-ratio "lobster-eye" and antiscatter collimators by deep x-ray lithography.

1.8.1 Spatial Coherence Measurement

The dream of creating intense, highly coherent x-ray beams is fueled by the tantalization of new coherence-based x-ray experiments, as well as by existing techniques, such as scanning microscopy, interferometry, coherent scattering, and phase measurement. Thus there is strong motivation